Theoretical and Applied Fracture Mechanics 133 (2024) 104561

Contents lists available at ScienceDirect

Theoretical and Applied Fracture Mechanics

journal homepage: www.elsevier.com/locate/tafmec

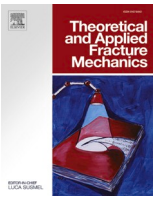

Exploiting small punch test for mechanical characterization of cold sprayed deposits

Asghar Heydari Astaraee, Kiran Tulasagiri Raddi, Sara Bagherifard, Chiara Colombo *

Department of Mechanical Engineering, Politecnico di Milano, Via La Masa 1, 20156 Milan, Italy

ARTICLE INFO

Keywords:
Small Punch Test
Inverse Analysis
Characterization
Cold Spray

ABSTRACT

Conventional testing procedures often encounter challenges to characterize the mechanical properties of deposits of limited thickness such as coatings. To overcome this limitation, the literature has explored various miniature-testing methods, and, among these, the small punch test has emerged as a promising solution offering the main advantage of requiring a minimal volume of material. This study focuses on cold sprayed deposits in as-sprayed and thermally treated conditions and presents the results of an experimental campaign of mechanical characterization of 316L steel and copper deposits. In parallel, small punch tests are simulated numerically with inverse analysis to estimate comprehensively the stress-strain curves. Results suggest an extremely brittle behavior of the as-sprayed specimens and a good agreement between the experimental and numerical estimations of the mechanical properties of the ductile thermally treated specimens. Ultimately, the findings highlighted the sensibility of the small punch test to the microstructure and its gradients of cold sprayed deposits.

1. Introduction

With the evolving demands of modern manufacturing, there is a growing need for advanced deposition techniques that not only enhance performance but also offer precision and efficiency in their application. Additive manufacturing (AM) has emerged as a major breakthrough in this arena. Among the different AM techniques, cold spray (CS) technology represents an innovative approach; it can be used not only as a coating methodology but also for AM and repair applications [1,2]. The material to be deposited, which is in the powder form, is accelerated to very high velocities (100–1000 m/s) by passing a pre-heated propellant gas through a specially designed converging–diverging nozzle. The powder particles deform upon impact and eventually bond to the surface, forming a very dense and strong deposit.

In comparison to thermal spray methods, CS is a solid-state process that eliminates the need to melt the deposited material, lowering the risk of undesired phase formation in the deposited material as well as thermal damage and oxidation of the substrate material [3]. CS deposits are also known for their high bonding strength, which is due to the high-velocity impacts of the powder particles during deposition [4]. Furthermore, CS high-density deposits are very resistant to wear and corrosion making them ideal to be used in harsh environments or applications under high mechanical loading [5]. CS offers a high build-rate and deposition efficiency and thus can reduce the overall cost of the manufacturing process [6,7]. As a result, CS has found successful applications in various industries such as the aerospace, automotive, and energy sectors.

Mechanical characterization of the deposits plays a vital role in optimizing the CS process and ensuring the reliability and performance of the components. However, mechanical characterization of the material using conventional testing methods, especially during the optimization of the manufacturing parameters, can be an expensive task due to the substantial amount of required material. The small punch test (SPT) is a recently standardized technique for mechanical characterization requiring extremely small specimen sizes. It is essentially a non-destructive mechanical testing method that involves clamping a thin disk-shaped specimen between two circular dies [8]. Using a hemispherical head punch, the specimen is stretched until the specified drop in maximum force is reached. The punch moves through the specimen at a constant displacement rate while the force exerted on the specimen is measured by a load cell located above the punch head. The displacement of the specimen can be measured using a clip gauge with knife edges mounted to the fixture or by the crosshead displacement. The force–displacement data are recorded during the test, and the resulting curve is used to calculate several material properties such as elastic modulus [9], yield stress [10], fracture toughness [11] and ultimate tensile strength [12]. Empirical formulas are used usually to derive the

* Corresponding author.
E-mail address: chiara.colombo@polimi.it (C. Colombo).

https://doi.org/10.1016/j.tafmec.2024.104561
Received 30 December 2023; Received in revised form 3 June 2024; Accepted 24 June 2024
Available online 25 June 2024

Nomenclature

ANC	Annealed Copper
ASC	As-Sprayed Copper
ASS	As-Sprayed Steel
AM	Additive manufacturing
CS	Cold Spray
EDS	Energy-Dispersive X-ray Spectroscopy
FE	Finite Element
HIPS	Hot Isostatic Pressed Steel
IA	Inverse analysis
MAE	Mean Absolute Error
NMAE	Normalized Mean Absolute Error
PEEQ	Equivalent Plastic Strain
SEM	Scanning Electron Microscopes
SPT	Small Punch Test
UTS	Ultimate Tensile Strength
YS	Yield Stress
A	Hollomon Constant
C_P	Punch Compliance
E	Elastic Modulus
E_m	SPT total energy
E_{PL}	SPT plastic energy
E_{SP}	SPT fracture energy
F	Force
F_e	SPT characteristic transition force
F_f	SPT characteristic final force
F_m	SPT characteristic maximum force
h_0	Initial Thickness
h_f	Final Thickness
K	Strength Coefficient
n	Strain Hardening Exponent
u	Specimen deflection
v	Punch displacement
v_e	Punch displacement corresponding to the force F_e
v_f	Punch displacement corresponding to the force F_f
v_m	Punch displacement corresponding to the force F_m
β_{UTS}	Material-dependent constant for UTS
β_{YS}	Material dependent constant for YS
ε_e	Engineering Strain
ε_f	Fracture Strain
ε_t	True Strain
σ_e	Engineering Stress
σ_t	True Stress

mechanical properties; however, at a more advanced level, numerical techniques such as inverse analysis (IA) combined with finite element (FE) modeling have been utilized to find the material constitutive parameters based on optimization procedures [13,14]. Different material constitutive models such as Hollomon [13–16], Ramberg-Osgood [17,18], and Ludwik models [19,20] have been attempted in this regard.

SPT has been used extensively to assess the properties of a broad range of materials, including metals, ceramics, polymers, and composites [11]. However, in recent years, there have been several attempts to investigate the potential of SPT for evaluating the mechanical integrity of materials produced by novel manufacturing techniques such as AM as well as depositions aimed at coating applications. The study by Lewis et al. [21] implemented SPT to characterize the fatigue performance of Ti-6Al-4 V and C263 nickel-based super alloy manufactured by electron beam melting and laser powder bed fusion and compared them to traditionally manufactured counterparts. The study successfully correlated microstructural morphologies with fatigue behavior and demonstrated the potential of SPT in evaluating the properties of AM materials. Courtright et al. [22] used SPT to evaluate Inconel 718 alloy manufactured by selective laser melting process where the effects of various build directions and post-processing heat treatments on mechanical properties were investigated. Chen et al. [23] used the SPT method showing great promise in evaluating the mechanical performance of thermally sprayed CoNiCrAlY coatings via vacuum plasma spraying. The study emphasized the importance of understanding the impact of coating defects, such as un-melted particles on mechanical behavior. The investigation discussed that the clamping process during the small punch test could induce micro-cracking around the defects before testing, with the un-melted particles serving as primary sites for cracking and fast failure within the coating. Wong et al. [24] performed fractographic studies on the Ti-6Al-4 V coatings produced by cold spray on a similar substrate using SPT at a temperature of 327 °C. The coating material showed brittle fracture behavior confirmed by fractographic investigations and microstructural analysis. The potential source for the dropped performance was attributed to the relatively high porosity level (3 % volume fraction).

The microstructure of materials deposited by CS is usually different in comparison to that of conventional bulk due to the existence of a large area of inter-splat regions possibly with unbonded or weakly bonded interfaces, an appreciable amount of defects such as pores and microcracks, and anisotropy in the deposited structure and thus in the mechanical properties. Thus, it is interesting to investigate the capability of the SPT for the mechanical characterization of such materials. This research aims to establish a framework for the mechanical characterization of deposits produced through the CS process, utilizing the SPT as the main mechanical testing method. To the authors' knowledge, this area of research on CS deposits has received limited attention. The fractographic investigation by Wong et al. [24] on a cold sprayed material has shown a bright prospect for SPT application in studying the mechanical integrity of the CS deposits. However, SPT can be a quantitative test, enabling the estimation of mechanical properties such as yield stress (YS) and ultimate tensile strength (UTS), which were not considered in the study by Wong et al [24].

The current study is composed of two main cores: performing SPT experiments and developing a robust IA procedure to use the SPT data for estimating the tensile behavior of the tested materials. The materials selected for CS deposition were 316L stainless steel and commercially pure copper that have been used extensively for AM and coating purposes by CS. The deposited materials were examined by SPT in as-sprayed and annealed conditions to highlight the effect of microstructural features induced by CS on mechanical properties. In this regard, microstructural characterization, microindentation and fractography were also implemented to reveal the relevant microstructures and local mechanical properties. A FE model was implemented to simulate the SPT; the optimization was performed as the core of the IA to obtain the optimal stress-plastic strain curve that provided the best fit between the numerical and experimental SPT data. The study was completed by analyzing the suitability of the empirical correlation suggested in the literature for the characterization of mechanical properties of CS deposits.

2. Experimental procedure

2.1. Specimen preparation

316L stainless steel and commercially pure copper powders were used to produce deposits with the CS technology. 316L stainless steel powder (Sandvik Osprey LTD, UK) produced by atomization process in a nitrogen atmosphere had a size distribution of d10 = 19 μm, d50 = 29 μm, and d90 = 44 μm measured using the Malvern 2000 instrument. Gas

atomized oxygen-free copper powder (Safina, CZ) had a particle size distribution of d10 = 13 μm, d50 = 23 μm, d90 = 46 μm, measured using a Malvern Morphologi 4 particle size analyzer (Malvern Panalytical Ltd, UK). CS deposition was carried out using an Impact Innovations ISS 5/11 CS system (Impact Innovations Inc., Germany) and 5/8 Impact high-pressure cold spray system (Impact Innovations, DE) for 316L steel and copper, respectively. In both cases, a convergent-divergent (de-Laval) OUT1 nozzle (Impact Innovations, Germany) with a length of 160 mm and an expansion ratio of 5.6 was employed. Nitrogen gas was used as a carrier and process gas. Table 1 shows the CS parameters for both materials.

CS deposits of 316L steel were produced with a thickness of 6 mm. Dog bone self-standing specimens of 100 mm long and 3 mm thick were then extracted from 316L deposits using electro-discharge machining. Static tensile tests were performed on these specimens using MTS Alliance RT/100 machine at a constant rate of 1 mm/min following the ISO 6892–1 standard as reported in a previous study [7]. Table 2 gives the tensile YS, UTS, and percent elongation data. In the case of copper specimens, 1 mm thick copper deposits were sprayed on a polymeric substrate of polyether ether ketone (PEEK) with parameters optimized in a previous study [25] as provided in Table 1. The deposits were easily detachable from the substrate since the adhesion strength was quite low.

The disc specimens required for the SPT were obtained for both materials using electro-discharge machining with a diameter of d = 8 ± 0.01 mm and a thickness h_0 slightly higher than 0.5 mm. Subsequently, grinding with SiC abrasive paper (P2500) was carried out to get h_0 within the specified tolerance value of 0.5 ± 0.005 mm and the prescribed roughness. The final disc dimensions were in accordance with ASTM E3205-20 [26].

316L steel discs included three conditions: (1) as-sprayed, (2) annealed at 1000 °C for 1 h using a heating rate of 30 °C/min followed by furnace cooling and (3) hot isostatic pressed (HIPed) at 1100 °C for 3 h with 1000 bar pressure using EPSI unit in argon atmosphere. Copper specimens were tested under two conditions: (1) as-sprayed and (2) annealed specimens at 400 °C for 1 h. Table 3 summarizes the number of specimens for 316L steel and copper and their coding. While the 316L specimens were extracted from the middles of the deposit, in the case of copper specimens we extracted them from the area close to the substrate to also evaluate the effect of distance from the substrate in the deposit properties. Two of the as-sprayed copper specimens, ASC-1 and ASC-2, were tested with the substrate side positioned opposite to the punch, and the other two specimens, ASC-3 and ASC-4, were tested with the substrate side positioned in contact with the punch. In the former the region close to the substrate was tested in tension, while in the latter it underwent compression loading.

2.2. Microstructural analysis and microhardness measurement

The microstructural analysis and microhardness measurement of the 316L steel deposits were performed in a previous study [7] and the relevant information will be reviewed in section 3.1 accordingly. The copper deposits were cross-sectioned, mounted into a resin, and ground with standard SiC abrasive papers using a metallographic polisher Mod MP311T. The specimen preparation was completed with polishing in successive steps of 6-, 3-, and 1-μm diamond paste, achieving a highly reflective surface. A Leitz Aristomet optical microscope (OM) and a Zeiss EV050 scanning electron microscope (SEM) equipped with an energy-dispersive X-ray spectroscopy (EDS) detection system were employed in the study for microstructural characterization. Etching was performed using 2 g of $FeCl_3$ and 5 ml of HCl in 20 ml of H_2O solution for 30 s to reveal the microstructure. The porosity of CS deposits in the as-sprayed and heat-treated specimens was evaluated by image analysis using ImageJ 1.49 software on the OM images in the polished condition.

Vickers microhardness tests were performed on the copper specimens to determine their microhardness using the Future-Tech FM-700 micro-indentation equipment. Each measurement used a 100 g load with a dwell duration of 15 s. For the as-sprayed specimens, hardness measurements were performed on the disc surfaces, both the substrate side and the opposite of the substrate side, as well as on the cross-section. For the annealed series, the measurements were carried out only on the cross-section. The measurements were repeated three times on each specimen to achieve reliable results.

2.3. SPT procedure

The SPT of the cold sprayed 316L steel specimens was conducted using an MTS Alliance RF/150 testing machine with a maximum capacity of 100 kN while for testing copper deposits, an MTS Synergie 200 testing machine with a load capacity of 1 kN was utilized. The test setup is shown in Fig. 1, where the punch and clamps (including upper and lower dies) were made of quenched and tempered 39NiCrMo3 steel. The receiving die bore diameter of the lower die is 4.00 ± 0.01 mm, the punch tip radius is 1.25 ± 0.01 mm, and the corner radius of the receiving die is 0.20 ± 0.05 mm. The device was designed following the standards ASTM E3205-20 [26] and EN 10371:2021 [27]. Similarly, the test procedures followed the standards, e.g. the loading rate was 0.5 mm/min and the tests were performed at room temperature. The test was programmed to stop when the load dropped by 20 % of the recorded maximum load.

Force and crosshead data were recorded during the SPT. The actual punch tip displacement v was calculated from the crosshead displacement v_c corrected by removing the punch compliance C_P using Eq. (1) [27]:

$$v = v_c - F(v_c) \bullet C_p \tag{1}$$

where, $F(v_c)$ is the force as a function of the crosshead displacement v_c. Once the force-punch displacement (F-v) data was obtained, the characteristic SPT parameters were extracted. For the sake of clarity, SPT

Table 2
Tensile properties of 316L steel obtained from standard dog-bone specimens [7].

	As-sprayed	Annealed	HIPed
YS [MPa]	687 ± 52	418 ± 3	347 ± 0.6
UTS [MPa]	723 ± 33	696 ± 6	672 ± 2.5
Elongation [%]	0.47 ± 0.02	49 ± 2	53 ± 1.2

Table 3
Summary of the test series carried out for 316L steel and copper.

Specimen material and condition	Specimen code	Number of tests
As-Sprayed 316L Steel	ASS	4
Annealed 316L Steel	ANS	4
HIPed 316L Steel	HIPS	4
As-Sprayed Copper	ASC	4
Annealed Copper	ANC	2

Table 1
Cold spray process parameters for 316L steel and copper depositions [25].

Material	Propellant gas	Stand-off distance (mm)	Hatching distance (mm)	Feed rate (g/min)	Gun speed (mm/s)	Pressure (MPa)	Temperature (°C)
316L steel	N_2	30	1	35	500	5	1100
Cu	N_2	40	2	25	30	4	300

Fig. 1. SPT experimental test setup.

standards consider the specimen deflection u as the reference displacement signal; however, when not directly measured, the punch displacement v, corrected with Eq. (1), may be used instead.

The main parameters used in the calculations are:

- F_e – Force characterizing the transition from elastic to plastic behavior,
- v_e – Punch displacement corresponding to F_e,
- F_m – Maximum force recorded during the SP test,
- v_m – Punch displacement corresponding to F_m,
- F_f – Final force corresponding to a 20 % force drop with respect to F_m,
- v_f – Punch displacement corresponding to F_f,
- E_{SP} – Fracture energy determined by the area under the F-v curve up to the displacement v_f,
- E_m – Total energy (Elastic + Plastic) determined by the area under the F-v curve up to the displacement v_m,
- E_{PL} – Plastic energy determined by the area under the F-v curve up to the displacement v_m.

In compliance with the ASTM 3205–20 standard, F-v curve was analyzed to calculate the characteristic parameters using a developed Python script. The YS and UTS were calculated based on the empirical correlation formulas (Eq. (2) and Eq. (3)) from the standard using the relevant characteristic SPT parameters [26]:

$$YS = \beta_{YS}\frac{F_e}{h_0^2} \tag{2}$$

$$UTS = \beta_{UTS}\frac{F_m}{h_0 v_m} \tag{3}$$

where h_0 is the initial specimen thickness.

At the end of the SPT, pictures of all specimens were collected from various angles using a Zeiss Discovery V12 stereomicroscope, both with top and bottom views and with cross-sectional views.

3. Numerical modelling

3.1. FE modelling

A FE model for the SPT was developed using Abaqus/Standard 2020 software to estimate the stress–strain curve of the deposits via the inverse methodology. Due to the simple geometry, an axisymmetric 2D modelling approach was followed. The punch and dies were modelled as discrete rigid bodies, while the disc specimen was modelled as a deformable body. These components were assembled with the punch tip in contact with the specimen surface and the specimen clamped between the dies as shown in Fig. 2a. The FE simulation was run using two successive static-general steps considering geometric nonlinearity. In the first step, a 10 kN force was applied to reference point 2 of the upper die to simulate the clamping force exerted by the dies on the specimen. The second step aimed to mimic the vertical downward movement of the punch towards the specimen. To achieve this, the punch vertical displacement was imposed at reference point 1 while all other translational and rotational degrees of freedom were fixed. An encastre constraint was imposed on the lower die to replicate the fixed boundary conditions of the test rig components.

The dies and punch were meshed using 2D rigid elements (RAX2), while the specimen was meshed with eight-node axisymmetric quadrilateral elements with reduced integration (CAX8R). A mesh convergence study was conducted by varying the number of elements from 75 to 1000. It was observed that beyond approximately 800 elements, there was no significant variation in the maximum PEEQ value. Therefore, all the simulations were carried out using a total of 800 elements with 0.05 mm edge size. A general contact was employed to define the interactions between surfaces. The friction coefficient for the steel pairs was set to 0.42 [28], while for the contact between copper and steel, it was set to 0.36 [29]. Eventually, the resulting reaction force and the applied displacement data were extracted using reference point 1 of the punch.

3.2. Material model

The elastic modulus values of 129800 MPa and 186000 MPa [30] were considered for copper and 316L steel, respectively. The Hollomon material model [16] was selected to describe the elastoplastic behavior of the materials, as given in Eq. (4):

$$\sigma = E\varepsilon \quad for\ \sigma < A$$

$$\sigma = E^n A^{1-n}\varepsilon^n \quad for\ \sigma > A \tag{4}$$

where σ is the true stress, ε is the true strain, E is the elastic modulus, A is the Hollomon constant, and n is the strain hardening exponent. The material constants A and n will be derived for the cold sprayed materials using the IA approach (section 2.8). Other material models were considered, e.g. Swift [31,32] and Ludwik models [19,20], but with less satisfactory results with respect to Hollomon.

3.3. Forward analysis

To validate the accuracy of the developed FE model of SPT, the uniaxial tensile properties of dog-bone 316L steel specimens were used as the material model input into the FE model, and the output force–displacement data were compared to the experimental SPT data. The experimental stress–strain data were fitted to the Hollomon equation using the least squares as the optimization procedure for three material conditions (Fig. 2b) and the fitted data were inserted in the FE model.

3.4. Inverse analysis

The objective of the numerical IA was to derive the stress–strain curves of the CS deposited material by fitting the experimental F-v data.

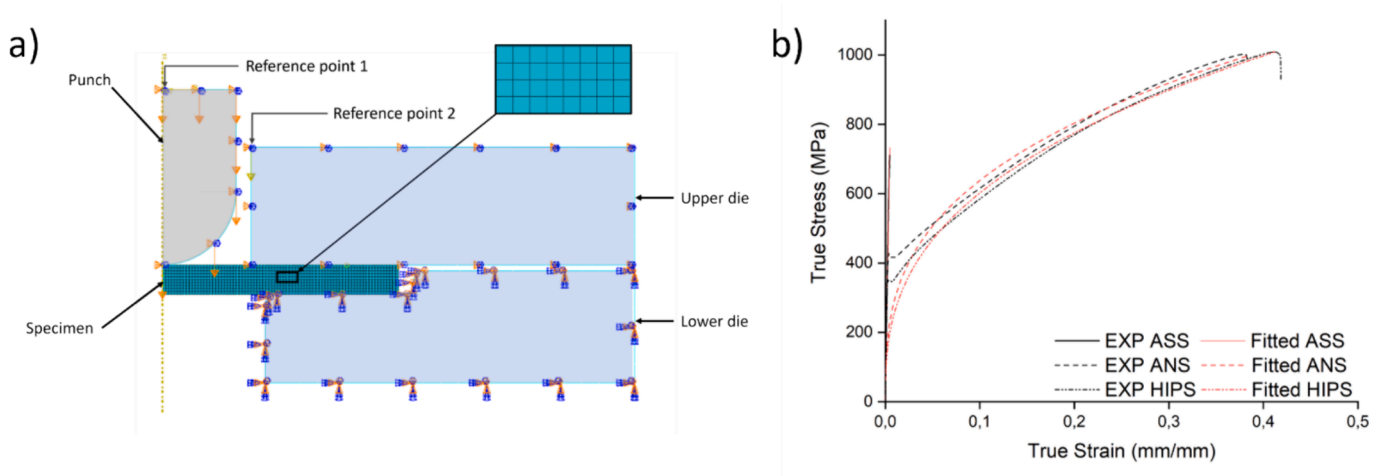

Fig. 2. (A) Fe model of SPT (b) experimental [7] and fitted true stress-strain of 316L steel obtained by tensile tests.

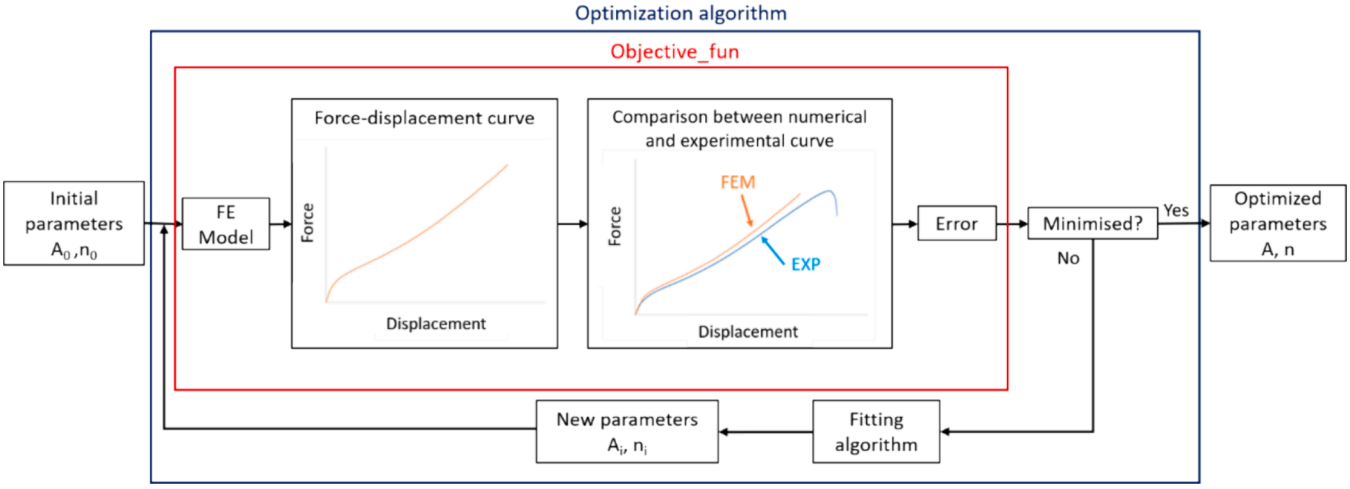

Fig. 3. Inverse analysis algorithm.

Fig. 3 shows the flowchart of the IA algorithm, which was developed in Python language to automatize the procedure. The algorithm started with a tentative set of Hollomon parameters, selected within a specified interval; they allowed computing the initial plastic properties and, through the FE simulation, computing the output F-v curve. This was then compared to the experimental F-v data, and their difference was quantified using mean absolute error (MAE) [33]. The normalized mean absolute error (NMAE) was determined by dividing the MAE by the average force. Then, the code conducted an iterative optimization using a least squares minimization function. The algorithm automatically changed the Hollomon law constants to reduce the difference between the experimental and numerical F-v curves. When the difference was below a threshold, the iterations ended, resulting in a well-fitted F-v curve and the optimized plastic material constants.

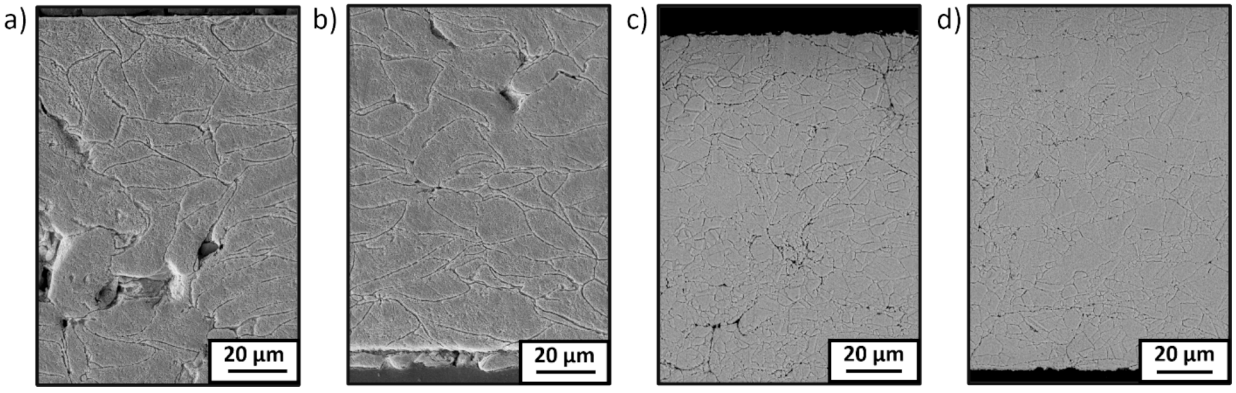

Fig. 4. Microstructure of the copper material a) far from and b) near to the substrate of as-sprayed condition (ASC-1), and c) far from and d) near to the substrate of annealed condition (ANC-2).

4. Results and discussion

4.1. Microstructural characterization

Fig. 4a shows the cross-sectional morphology of deposited copper near the top surface, with the top side corresponding to the top surface of the disc while Fig. 4b shows the deposition near the substrate, with the bottom side corresponding to the bottom side of the disc (and thus the substrate side). It can be observed that the particles near the substrate exhibit a more flattened and denser shape compared to those further away. This is because of the phenomenon commonly referred to as the tamping effect [34]. The initial particles effectively adhere to the substrate, forming the primary coating layer. Subsequently, the next particles collide continuously with the previously deposited particles resulting in more densification and work hardening. In order to determine the flattening ratio, the width of the deformed particle was divided by the height of the deformed particle [35]. The evaluation revealed that the average flattening ratio near the substrate was 2.55 ± 0.19, while it was 2.17 ± 0.12 in the region far from the substrate. These findings provide evidence of the tamping effect, as particles in close proximity to the substrate exhibited a higher degree of flattening compared to those located far from it.

Fig. 4c illustrates the cross-sectional microstructure of the annealed copper near the top surface of the disc, with the top side away from the substrate while Fig. 4d depicts the deposition near the substrate, with the bottom side closer to the substrate. At first sight, the difference between the top and bottom is not as evident as in the case of the as-sprayed condition. By comparing Fig. 4a and c, it could be inferred that new grains were formed upon annealing at 400 °C for 1 h. This can be attributed to the recrystallization phenomenon, which led to nucleation and growth of new grains out of the initially deformed structures and thus led to a change in the morphology of structures following annealing.

A detailed investigation of the microstructure for 316L steel depositions can be found in a previous study [7]. The average particle flattening ratio of 2.77 ± 0.09 was detected for the as-sprayed 316L steel. Heat-treated 316L steel displayed a more uniform microstructure with recrystallized grains compared to the as-sprayed condition. HIPed 316L steel showed even more regular and completely recrystallized microstructure.

The corresponding porosity for CS-deposited copper and 316L steel is depicted in Fig. 5a. A reduction in porosity was found upon annealing. This decrease in porosity can be attributed to various factors, such as the removal of residual gases and trapped air, particle rearrangement, and interface bonding through inter-diffusion, resulting in the filling of void spaces and eventually decreasing porosity [36]. The HIP treatment for 316L steel resulted in an even greater reduction of porosity due to the atomic diffusion at the splat interfaces because of the high temperature accompanied by the isostatic pressure [7]. It is observed that the selected CS processing parameters were able to produce depositions with a very limited porosity in the as-sprayed condition. This porosity could be further reduced with thermal/mechanical treatments.

Vickers microhardness test results are shown in Fig. 5b for all the material conditions. Following the post-treatment processes, the hardness decreased to around half for both 316L steel and copper compared to the respective as-sprayed condition. The difference can be related to the recrystallization during the post-treatments confirmed by the microstructural observations (Fig. 4), resulting in a decrease in the material's hardness. The HIP treatment decreased the hardness further with respect to annealing, in line with the detected microstructure [7]. As regards the as-sprayed copper, the hardness on the bottom surface was found to be higher compared to the top surface. This observation is in accordance with the variation in the flattening ratio and can be attributed to the tamping effect during deposition, indicating a higher work hardening near the substrate side.

4.2. SPT results

Fig. 6a shows the SPT plot of load cell force (F) vs corrected tip displacement (v) for the as-sprayed, annealed, and HIPed 316L steel specimens. The results highlight a relatively good repeatability for the performed tests. An overall different force–displacement behavior was observed for the three considered conditions. The slope of the as-sprayed data is steeper than that of the annealed one. Besides, the as-sprayed condition shows a lower maximum force and a lower corresponding v-displacement at failure; this confirms a more brittle behavior of the as-sprayed material and inferior plastic deformation capacity. On the other hand, the annealed specimens exhibit a more gradual increase in force with displacement, indicating higher ductility and/or strength [37]. The HIP treatment on 316L steel further enhanced both the maximum force and the corresponding displacement compared to the annealed state. This is because the HIP treatment is not only able to increase the ductility, due to a more homogeneous and fully recrystallized structure but also reduce further the porosities in the cold-sprayed material, which lowers the risk of premature failure during mechanical tests [7].

Fig. 6b depicts the SPT force–displacement results for the copper specimens. Regarding the effect of the annealing post-treatment, the results show a trend similar to the case of 316L steel. Annealing contributes to an increase in both the maximum force and the corresponding displacement achieved in copper specimens. The SPT data is found to be

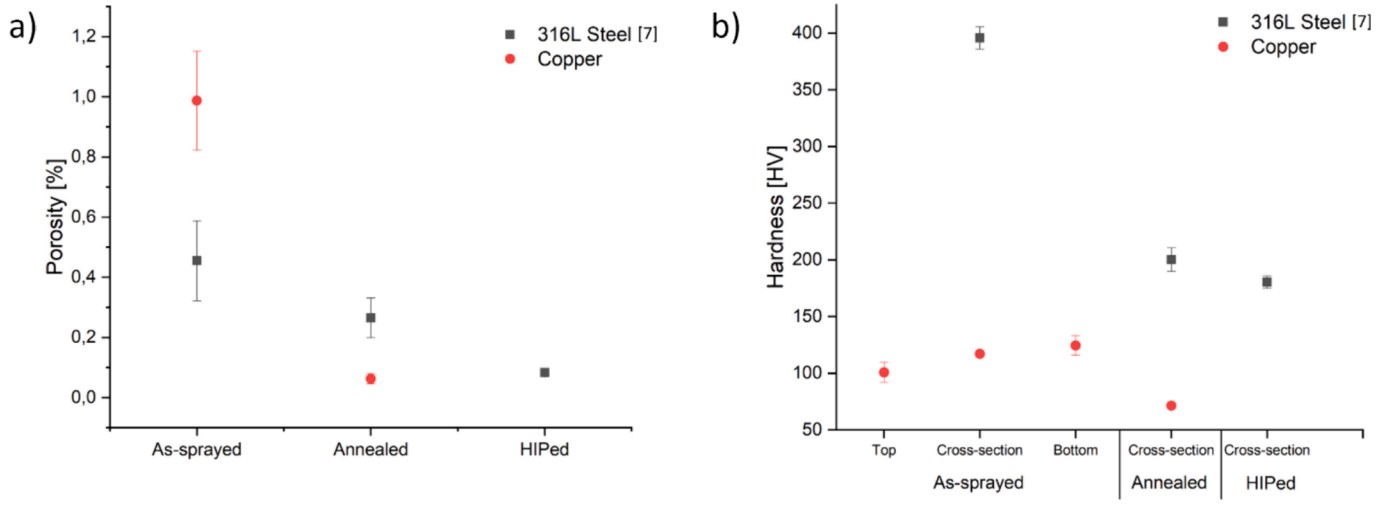

Fig. 5. Results of a) porosity analysis and b) microhardness obtained through Vickers micro-indentation test.

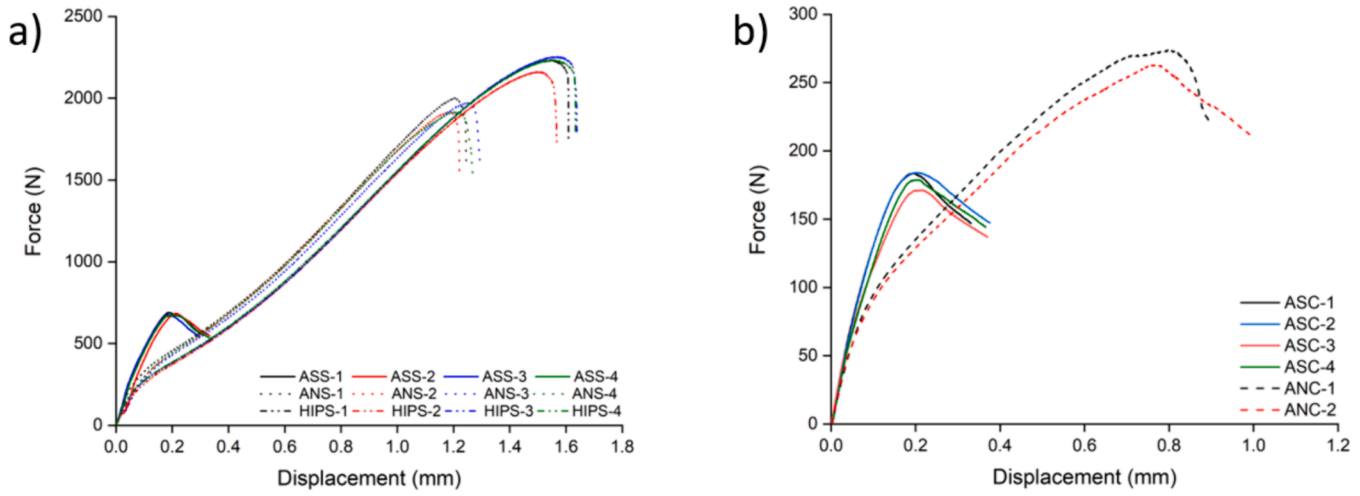

Fig. 6. Force-displacement plots of a) 316L Steel and b) copper specimens.

sensitive to the small variations in the material properties and, ultimately, to the microstructure. A small discrepancy is found among the load–displacement curves for each material condition. Slightly lower force–displacement curves were recorded for the as-sprayed copper for which the side closer to the substrate during deposition was in contact with the punch (ASC-3 and ASC-4 specimens) with respect to the opposite side of the specimen when in contact with the punch (ASC-1 and ASC-2 specimens). For the annealed copper, the observed discrepancy between the two specimens was not investigated in detail but most probably was due to the intrinsic variations of the microstructure.

Table 4 summarizes the average SPT characteristic parameters for 316L steel and copper. A distinct transition between elastic and plastic regions was not detected for the as-sprayed conditions due to the apparently brittle deformation behavior. Hence, the relevant F_e, v_e and E_{PL} parameters are not listed in the table. However, both annealed and HIPed conditions with ductile behavior showed a clear elastic–plastic zone transition [38].

4.3. Empirical correlations

Table 5 gives the constants β_{YS} and β_{UTS}, calculated based on the empirical correlations (Eq. (2) and Eq. (3)), using the 316L steel material characteristic parameters and the corresponding tensile properties (Table 2). It is worth noting that an identical approach was not possible for CS copper since tensile test data on dog-bone specimens was not available.

Referring to 316L steel, the range of β constants for metallic materials and steels from literature is also included in Table 2. β_{YS} of the cold-sprayed 316L steel in the annealed and HIPed conditions matches well with the literature data. This match is still good when comparing the results for β_{UTS}. However, a much lower (almost half) β_{UTS} constant for the as-sprayed 316L steel was detected compared to other heat-treated conditions. The reason for such a low constant can be discussed based on the microstructural features evident in the as-sprayed condition. Under tensile loading, a work-hardened and less ductile matrix together with a large volume of unbonded interfaces, micropores, and porosities will lead to a premature failure and thus a low UTS. However, annealing facilitates the transition of the cold-sprayed material towards a microstructure normally found in conventional materials.

Moreover, this difference in β_{UTS} suggests that literature values of the empirical correlation may not be fully applicable to the as-sprayed 316L deposit. Besides, the use of empirical correlations for conventional materials is still debated in the literature. Some researchers [39,40] have proposed that the β_{YS} and β_{UTS} constants are universal and valid for most conventional materials. However, F_m is probably not the most suitable parameter to correlate with UTS. For instance, the work by Altstadt et al.

Table 5
Correlation constants.

Material	β_{YS}	β_{UTS}	Data source
As-sprayed 316L	–	0.107	Current study
Annealed 316L	0.378	0.217	Current study
HIPed 316L	0.440	0.233	Current study
Austenitic stainless steel	0.477	–	Xu and Zhao [41]
Metallic materials	0.346 (R^2 = 0.92)	0.277 (R^2 = 0.94)	Garcia [42]
Steel	0.36–0.41	–	Finerelli [43]
Metallic materials	0.479	0.179	EN 10371:2021 [27]

Table 4
Average characteristic SPT parameters (N.A.: not available).

	316L Steel			Copper	
	As-sprayed	Annealed	HIPed	As-sprayed	Annealed
F_m [N]	681.25 ± 7.18	1952.23 ± 42.80	2221.78 ± 40.19	179.59 ± 6.00	268.71 ± 7.86
v_m [mm]	0.201 ± 0.013	1.212 ± 0.029	1.541 ± 0.026	0.209 ± 0.008	0.790 ± 0.024
F_f [N]	545.00 ± 5.72	1562.00 ± 34.22	1777.30 ± 32.31	143.50 ± 4.73	215.00 ± 5.66
v_f [mm]	0.320 ± 0.016	1.257 ± 0.032	1.611 ± 0.031	0.365 ± 0.020	0.953 ± 0.069
F_e [N]	N.A.	280.75 ± 22.53	198.50 ± 14.06	N.A.	84.20 ± 4.95
v_e [mm]	N.A.	0.090 ± 0.021	0.059 ± 0.013	N.A.	0.087 ± 0.004
E_{SP} [J]	0.1563 ± 0.0072	1.3308 ± 0.0470	1.9840 ± 0.0875	0.0493 ± 0.0030	0.1815 ± 0.0092
E_m [J]	0.0828 ± 0.0050	1.2475 ± 0.0404	1.8315 ± 0.0715	0.0238 ± 0.0005	0.1420 ± 0.0113
E_{PL} [J]	N.A.	0.6833 ± 0.0982	1.1773 ± 0.1577	N.A.	0.1085 ± 0.0092
ε_f [%]	0.54 ± 0.1	18 ± 4	31 ± 3	0.67 ± 0.2	13.6 ± 2

[40] carried out tests and simulations on ferritic-martensitic Cr-steels and bainitic steels, and suggested using the force when the punch displacement is $1.29 \bullet h_0$ instead of F_m for the correlation with the UTS and the calculation of β_{UTS}. Therefore, especially because the materials in the present study are manufactured by an emerging deposition technique, it is important to apply advanced methods such as the inverse FE-modelling to thoroughly investigate the effective material behavior and extract the tensile properties from the SPT.

4.4. SPT specimen failure

Fig. 7 depicts the final failure due to SPT for both 316L steel and copper disc specimens. In the as-sprayed condition, radial patterns were observed on the fracture surface of both materials, indicating the presence of crack nucleation and propagation along the radial direction (Fig. 7a and d). The radial pattern observed on the fracture surface is a characteristic feature associated with brittle materials [44]. It suggests the propagation of cracks through the material, finally leading to failure. The observed features align with the behavior of brittle materials when subjected to localized loads [38]. Fig. 7b and e show the fractured nature of 316L steel and copper specimens in the annealed condition, respectively. Circumferential cracks are visible on the surface indicating its ductile fracture behavior. Furthermore, the presence of a visible bulge in the specimens shows that there was significant plastic deformation before the failure. Fig. 7c represents the final fracture in a 316L steel HIPed specimen, where the deformation was similar to that of the annealed specimen.

Fig. 8a shows the cross-section of the SPT tested specimen for the as-sprayed copper while Fig. 8b depicts a closer view of the failure origin. It is observed that crack propagation followed an inter-splat path. This most probably stems from the fact that the inter-splat boundaries are the weakest regions in the sprayed structure due to the unbonded or weakly bonded interfaces [45]. These findings highlight the role of adhesive interactions on the brittle fracture behavior and crack propagation for the CS depositions.

The fracture strain parameter, as provided in Table 4, was evaluated using Eq.5 [26]:

$$\varepsilon_f = ln\frac{h_0}{h_f} \tag{5}$$

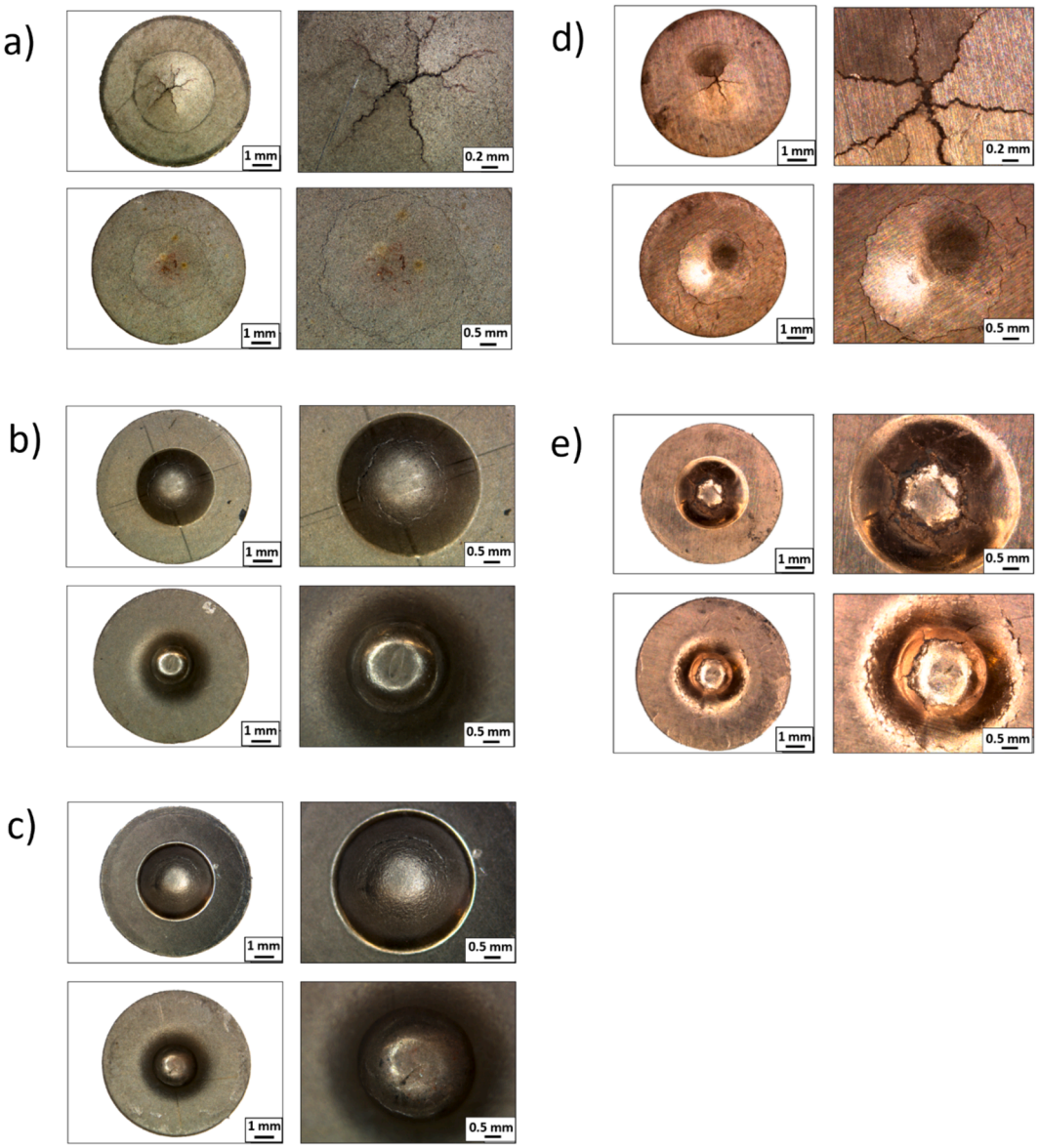

Fig. 7. Deformed and fractured specimen a) as-sprayed steel (ASS-2) b) annealed steel (ANS-1) c) HIPed steel (HIPS-1) d) as-sprayed copper (ASC-1) e) annealed copper (ANC-2).

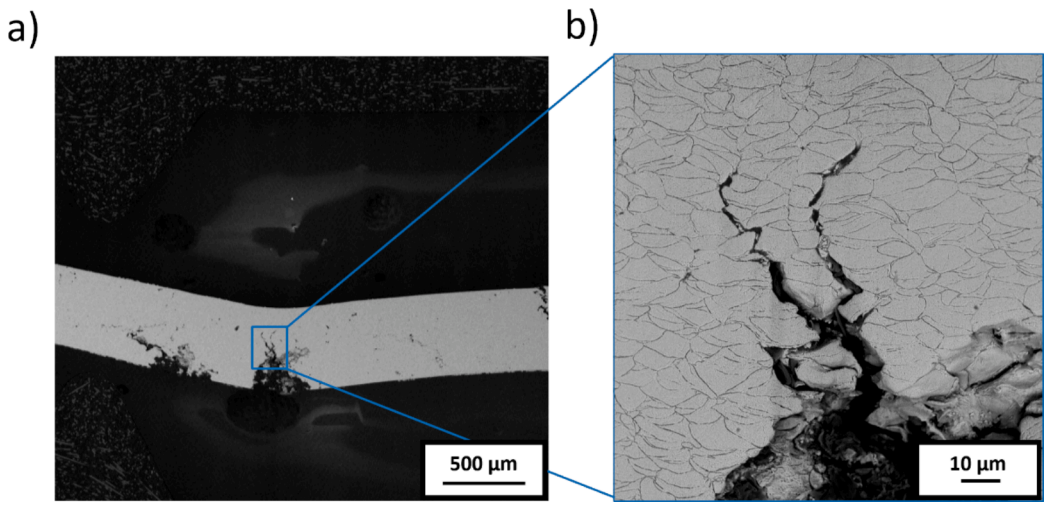

Fig. 8. Crack propagation in as-sprayed copper (ASC-1).

where ε_f is the fracture strain, h_0 is the initial thickness and h_f is the final thickness of the specimen adjacent to the failure region. The fracture strain increases from the as-sprayed condition to the post-treated conditions for both materials, signifying an enhanced ability to withstand deformation before failure. These results can be compared with the elongation obtained by tensile testing provided in Table 2. A relatively good match is obtained for the as-sprayed condition (0.47 % vs. 0.54 %) while the agreement decreased for the annealed (49 % vs. 18 %) and HIP (53 % vs. 31 %) conditions. This can be attributed partially to the effect of biaxial stresses developed in SPT on ductile failure while it is less affected when the material behavior is brittle.

4.5. SPT model validation

Fig. 9 represents the comparison of the force–displacement plots between the experiments and numerical results for 316L steel in various conditions (ASS-1, ANS-1, HIPS-1) obtained through forward analysis (section 2.7). The results show a very good agreement between the numerical and the experimental force–displacement data. This validates the sufficient accuracy of the developed FE model in simulating the SPT. It is noted that there is a deviation between the experimental and the numerical force–displacement curves close to the maximum load where the initiation and propagation of the damage occurs. This was expected since the developed FE simulation did not include any material damage models and, thus, was not able to capture damage initiation.

4.6. Inverse analysis results

4.6.1. Inverse analysis convergence

The experimental data for 316L steel HIPed was used to validate the IA procedure. The IA was carried out using different starting points in

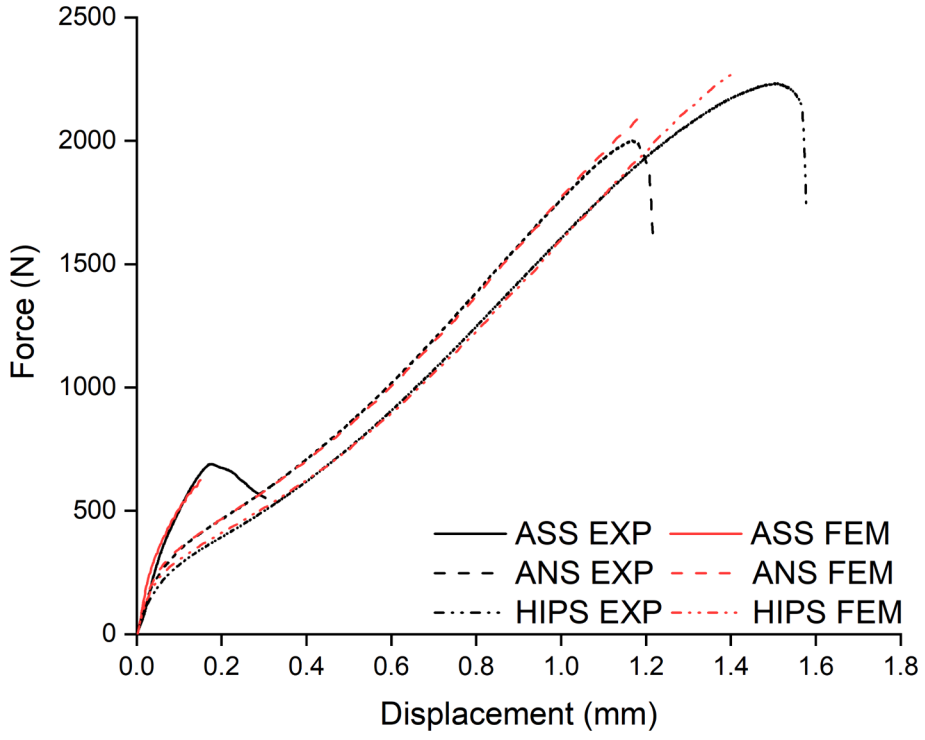

Fig. 9. Force-displacement curves of SPT for 316L steel: experimental data compared with the results of the forward analysis.

terms of A and n, corresponding to the extreme values of the interval where the solution is sought. Table 6 presents the results where it is evident that all four trials converged toward the same solution. This convergence indicated that the optimization code was functioning correctly and effectively.

4.6.2. 316L steel inverse analysis results

Fig. 10a shows the quality of the fitting by IA for all three 316L steel variants. The fitted curves exhibit a good alignment with the experimental ones. The difference between numerical and experimental load–displacement curves is quantified by the NMAE. The error of the as-sprayed curve (7.42 %) is higher than that of the annealed (0.65 %) and HIP curves (1.20 %). This higher error could be related to the limitations of the Hollomon law in accurately representing the as-sprayed material, which shows a very brittle behavior. The resultant Hollomon law constants obtained by fitting are provided in Table 7 together with the Hollomon-fitted material parameters of the experimental data. Fig. 10b shows engineering stress–strain plots obtained from the IA plotted together with the experimental data. The results align fairly well with the experimental ones. The existing discrepancy can be attributed to the less flexible material model of Hollomon with only two constant parameters to describe the full stress–strain behavior.

Table 8 gives the 0.2 % offset YS and the UTS by IA along with the corresponding experimental tensile test data for 316L steel. The UTS of the as-sprayed conditions was specified based on the calculated fracture strain using empirical formulas (Table 4), while for the ductile conditions, the maximum obtainable stress was considered as the UTS. IA was unable to detect any YS for the as-sprayed material since a 0.2 % offset line did not cross the stress–strain curve. However, as also confirmed by the tensile test data, the YS and UTS of these series overlap considering the tolerances. The estimated YS by IA for the post-treated conditions did not match well with the experimental tensile ones most probably due to the limited capability of the Hollomon model in capturing the stress–strain behavior for small plastic strains. This is evident in Fig. 2b for the fitted stress–strain data. The UTS values estimated by IA for all material conditions demonstrate a good alignment with the experimental values, although for the HIP condition there appears to be more discrepancy.

4.6.3. Copper inverse analysis results

Fig. 11a shows the fitting quality for the deposited copper in the as-sprayed (ASC-1) and annealed (ANC-1) conditions. The error of fitting (NMAE) for the as-sprayed and annealed copper was calculated to be 10.8 % and 5.0 %, respectively. These are acceptable although they seem relatively high with respect to the ones for 316L steel indicating a less successful fitting of the numerical data on the experimental ones. It is hypothesized that the Hollomon model was less capable of capturing the deformation behavior of cold-sprayed copper. Fig. 11b illustrates the resultant engineering stress–strain curves, and the estimated Hollomon model parameters are provided in Table 7. Table 9 presents the magnitudes of YS (0.2 % offset) and UTS obtained using the stress–strain curves in Fig. 12b. The same methodology of calculations used for 316L were used here, i.e., the UTS was estimated based on the fracture strain for the as-sprayed condition and based on the maximum stress for the annealed condition. In this table, the estimated values of the mechanical properties using empirical formulas (section 4.3) are also provided. It is noted that there are no original data for the mechanical properties of the CS copper deposits using any conventional mechanical testing method such as tensile testing. Thus, the β constants in empirical formulas are not available for the specific copper deposits. For such calculations, the β constants obtained for cold sprayed 316L steel were used as a first approximation. The IA demonstrated a YS lower than the empirical correlation (about 26 % lower). However, the uncertainty in the calculation of YS can be large due to the limited capacity of the Hollomon model at low plastic strains. On the other hand, the UTS values of both the as-sprayed and annealed copper obtained from the IA align well with the ones obtained from the empirical correlation formulas.

Karmakar et al. [46] conducted tensile tests on pure copper cold sprayed at a pressure of 3.2 MPa and a gas temperature of 500 °C. They reported a YS = 170 MPa and a UTS = 195 MPa for the as-sprayed condition and a YS = 118 MPa and a UTS = 156 MPa for the annealed copper at 400 °C averaged for the two directions in the plane perpendicular to the build direction. In spite of some minor differences among the CS processing parameters, these results show a very good agreement with the results obtained in the current study highlighting the validity of the methodology proposed for the IA. It is noted that, however, the processing parameters of cold spray and the resultant microstructures may influence the magnitude of the mechanical properties. For example, Huang et al. [47] sprayed pure copper deposits at a gas pressure and temperature of 3 MPa and 800 °C and performed annealing at various temperatures including 400 °C. The as-sprayed material showed a UTS of around 300 MPa while annealing decreased it to around 200 MPa. Most probably, a higher spray temperature resulted in a stronger deposit compared to the current study. This, in turn, indicates that the estimation of UTS in the as-sprayed condition using empirical formulas can be sensitive to the CS processing parameters and thus, it is suggested to be proved by other approaches such as mechanical property estimation using IA, similar to the framework proposed in the current study.

5. Conclusion

In this study, an inverse analysis methodology was developed and proved to be successful in estimating the stress–strain behavior of free-standing cold sprayed deposits. Particularly, the following conclusions can be drawn:

- The small punch test characterized successfully cold sprayed deposits. From the experimental results, it is possible to conclude that the small punch test is suitable for identifying the effect of the thermal treatment compared to its initial as-sprayed state. Furthermore, the small punch test exhibits the capability to differentiate between ductile and brittle material behavior based on specific material conditions, such as the presence or absence of the F_e parameter.
- The results by inverse analysis provide compelling evidence of the effectiveness of the approach, particularly through its application to both 316L steel and copper materials.
- A connection was found between the results of the empirical correlation approach and the outcomes of the inverse analysis, providing validation and insights into the mechanical properties of cold sprayed deposits. Notably, the ultimate tensile strength values obtained through inverse analysis exhibited a strong agreement with those derived from empirical correlation formulas. This consistency underscores the reliability of the inverse analysis approach in estimating the tensile strength of the tested materials, thus validating its

Table 6
Convergence results for the inverse analysis.

Trials	1		2		3		4	
Constants	A [MPa]	n	A [MPa]	n	A [MPa]	n	A [MPa]	n
Starting point	100	0.2	250	0.2	100	0.5	250	0.5
Ending point	137.5	0.298	138.3	0.300	141.6	0.294	140.2	0.298

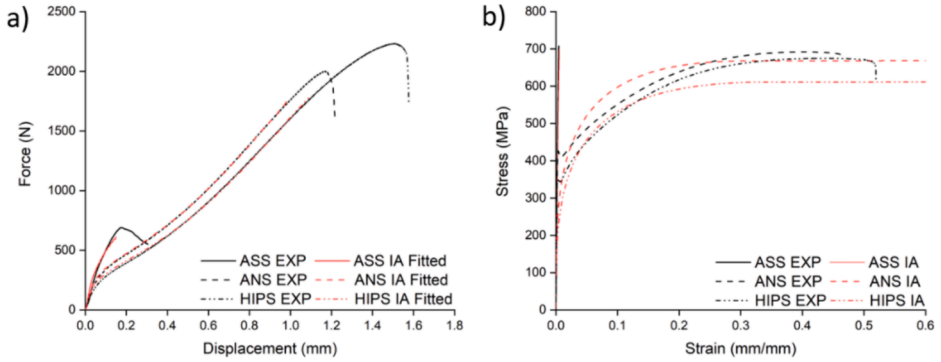

Fig. 10. Results of the inverse analysis on 316L steel: (a) force-displacement and (b) stress–strain curves.

Table 7
Material parameters of 316L steel and copper.

Steel Specimens	316L Steel						Copper			
	As-sprayed		Annealed		HIPed		As-sprayed		Annealed	
Constants	A [MPa]	n	A [MPa]	n	A [MPa]	n	A [MPa]	n	A [MPa]	n
Hollomon fitting	127.7	0.905	119.98	0.332	84.09	0.364	–	–	–	–
IA	78.71	0.846	186.89	0.275	135.63	0.300	10.09	0.672	72.27	0.142

Table 8
YS and UTS of 316L steel.

	YS [MPa]			UTS [MPa]		
	As-sprayed	Annealed	HIPed	As-sprayed	Annealed	HIPed
Experimental	687 ± 52	418 ± 3	347 ± 0.6	723 ± 33	696 ± 6	672 ± 2.5
IA	–	276	221	697	688	611

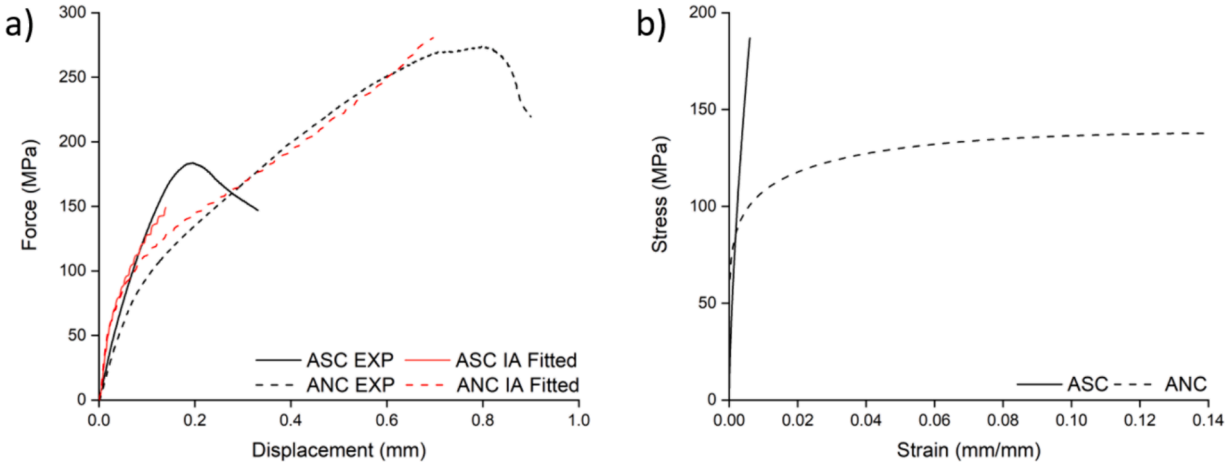

Fig. 11. Results of the inverse analysis on copper: (a) force-displacement and (b) predicted engineering stress–strain curves.

Table 9
YS and UTS obtained for copper deposits.

	YS [MPa]	UTS [MPa]	
	Annealed	As-sprayed	Annealed
Empirical correlations	125.9	183.1	146.8
IA	93.0	187.1	137.7

accuracy as a tool for characterizing material stress–strain behavior. However, the choice of Hollomon material model with only two constants restricted the prediction of yield stress by inverse analysis in the post-treated conditions.

CRediT authorship contribution statement

Asghar Heydari Astaraee: Writing – review & editing, Writing – original draft, Visualization, Validation, Supervision, Software, Methodology, Investigation, Formal analysis, Data curation, Conceptualization. **Kiran Tulasagiri Raddi:** Writing – original draft, Validation,

Software, Investigation, Formal analysis, Data curation. **Sara Bagherifard:** Writing – review & editing, Visualization, Supervision. **Chiara Colombo:** Writing – review & editing, Writing – original draft, Visualization, Validation, Supervision, Project administration, Methodology, Investigation, Funding acquisition, Formal analysis, Data curation, Conceptualization.

Declaration of competing interest

The authors declare that they have no known competing financial interests or personal relationships that could have appeared to influence the work reported in this paper.

Data availability

Data will be made available on request.

Acknowledgments

This work was carried out at Politecnico di Milano as part of the COSMEC (Cold Spray of Metal-to-Composite) project supported by the Italian Ministry for the Research (MUR), under the call ‘‘PRIN 2017’’, grant number 2017N4422T. KTR and SB acknowledge funding from the European Research Council (ERC) under the European Union’s Horizon 2021 research and innovation programme (ArcHIDep ERC-Co project, grant agreement n. 101044228). Open Access Funding was provided by Politecnico di Milano within the CRUI-CARE Agreement.

References

[1] S. Yin, P. Cavaliere, B. Aldwell, R. Jenkins, H. Liao, W. Li, R. Lupoi, Cold spray additive manufacturing and repair: fundamentals and applications, Addit. Manuf. 21 (2018) 628–650, https://doi.org/10.1016/j.addma.2018.04.017.
[2] G. Prashar, H. Vasudev, A comprehensive review on sustainable cold spray additive manufacturing: State of the art, challenges and future challenges, J. Clean Prod. 310 (2021) 127606, https://doi.org/10.1016/j.jclepro.2021.127606.
[3] R.F. Vaz, A. Garfias, V. Albaladejo, J. Sanchez, I.G. Cano, A Review of advances in cold spray additive manufacturing, Coatings 13 (2023) 267, https://doi.org/10.3390/coatings13020267.
[4] S. Singh, R.K.S. Raman, C.C. Berndt, H. Singh, Influence of cold spray parameters on bonding mechanisms: a review, Metals (basel) 11 (2021) 2016, https://doi.org/10.3390/met11122016.
[5] S. Bagherifard, M. Guagliano, Fatigue performance of cold spray deposits: Coating, repair and additive manufacturing cases, Int. J. Fatigue 139 (2020) 105744, https://doi.org/10.1016/J.IJFATIGUE.2020.105744.
[6] R. Ghelichi, M. Guagliano, Coating by the Cold Spray Process: a state of the art, Frattura Ed Integrità Strutturale 3 (2009) 30–44, https://doi.org/10.3221/IGF-ESIS.08.03.
[7] S. Bagherifard, J. Kondas, S. Monti, J. Cizek, F. Perego, O. Kovarik, F. Lukac, F. Gaertner, M. Guagliano, Tailoring cold spray additive manufacturing of steel 316 L for static and cyclic load-bearing applications, Mater. Des. 203 (2021) 109575, https://doi.org/10.1016/j.matdes.2021.109575.
[8] R.C. Hurst, R.J. Lancaster, S.P. Jeffs, M.R. Bache, The contribution of small punch testing towards the development of materials for aero-engine applications, Theoret. Appl. Fract. Mech. 86 (2016) 69–77, https://doi.org/10.1016/j.tafmec.2016.07.013.
[9] J. Calaf Chica, P.M. Bravo Díez, M. Preciado Calzada, Improved correlation for elastic modulus prediction of metallic materials in the Small Punch Test, Int. J. Mech. Sci. 134 (2017) 112–122, https://doi.org/10.1016/j.ijmecsci.2017.10.006.
[10] J. Kameda, X. Mao, Small-punch and TEM-disc testing techniques and their application to characterization of radiation damage, J. Mater. Sci. 27 (1992) 983–989, https://doi.org/10.1007/BF01197651.
[11] M. Abendroth, M. Kuna, Identification of ductile damage and fracture parameters from the small punch test using neural networks, Eng. Fract. Mech. 73 (2006) 710–725, https://doi.org/10.1016/j.engfracmech.2005.10.007.
[12] X. Mao, H. Takahashi, Development of a further-miniaturized specimen of 3 mm diameter for tem disk (ø 3 mm) small punch tests, J. Nucl. Mater. 150 (1987) 42–52, https://doi.org/10.1016/0022-3115(87)90092-4.
[13] M. Abendroth, FEM analysis of small punch tests, Key Eng. Mater. 734 (2017) 23–36, https://doi.org/10.4028/www.scientific.net/KEM.734.23.
[14] K. Li, J. Peng, C. Zhou, Construction of whole stress-strain curve by small punch test and inverse finite element, Results Phys. 11 (2018) 440–448, https://doi.org/10.1016/j.rinp.2018.09.024.
[15] R.J. Lancaster, S.P. Jeffs, B.J. Haigh, N.C. Barnard, Derivation of material properties using small punch and shear punch test methods, Mater. Des. 215 (2022) 110473, https://doi.org/10.1016/j.matdes.2022.110473.
[16] J.R. Hollomon, Tensile deformation, Metall. Soc. AIME 162 (1945) 268–290.
[17] S. Tu, X. Ren, J. He, Z. Zhang, Stress–strain curves of metallic materials and post-necking strain hardening characterization: A review, Fatigue Fract. Eng. Mater. Struct. 43 (2020) 3–19, https://doi.org/10.1111/ffe.13134.
[18] J. Isselin, A. Iost, J. Golek, D. Najjar, M. Bigerelle, Assessment of the constitutive law by inverse methodology: Small punch test and hardness, J. Nucl. Mater. 352 (2006) 97–106, https://doi.org/10.1016/j.jnucmat.2006.02.076.
[19] Y. Cao, Y. Zu, Y. Zhen, F. Li, G. Wu, Determination of the true stress-strain relations of high-grade pipeline steels based on small punch test correlation method, Int. J. Press. Vessel. Pip. 199 (2022) 104739, https://doi.org/10.1016/j.ijpvp.2022.104739.
[20] J. Calaf Chica, P. Bravo Díez, M. Preciado Calzada, A New Prediction Method for the Ultimate Tensile Strength of Steel Alloys with Small Punch Test, Materials 11 (2018) 1491. Doi: 10.3390/ma11091491.
[21] D.T.S. Lewis, R.J. Lancaster, S.P. Jeffs, H.W. Illsley, S.J. Davies, G.J. Baxter, Characterising the fatigue performance of additive materials using the small punch test, Mater. Sci. Eng. A 754 (2019) 719–727, https://doi.org/10.1016/J.MSEA.2019.03.115.
[22] Z.S. Courtright, N.P. Leclerc, H.N. Kim, S.R. Kalidindi, Critical Comparison of Spherical Microindentation, Small Punch Test, and Uniaxial Tensile Testing for Selective Laser Melted Inconel 718, Applied Sciences 2021, Vol. 11, Page 1061 11 (2021) 1061. Doi: 10.3390/APP11031061.
[23] H. Chen, A. Rushworth, W. Sun, J. He, H. Guo, Some considerations in using the small punch testing for thermally sprayed CoNiCrAlY coatings, Surf Coat Technol 357 (2019) 684–690, https://doi.org/10.1016/J.SURFCOAT.2018.10.080.
[24] A. Wong, Y.L. Tan, M. Pilot, R.J. Lancaster, S.P. Jeffs, F. Li, A.W.Y. Tan, W. Sun, E. Liu, I. Mitchell, Application of the small punch test to evaluate the integrity of a cold spray titanium coating, Ubiquity Proceedings 1 (2018) 47, https://doi.org/10.5334/UPROC.47.
[25] A. Heydari Astaraee, C. Colombo, S. Bagherifard, Insights on metallic particle bonding to thermoplastic polymeric substrates during cold spray, Scientific Reports 2022 12:1 12 (2022) 1–14. Doi: 10.1038/s41598-022-22200-5.
[26] ASTM E3205 Standard Test Method for Small Punch Testing of Metallic Materials, (2020). https://www.astm.org/e3205-20.html (accessed December 30, 2023).
[27] British Standards Institution, BS EN 10371:2021 Metallic materials - Small punch test method, EN 10371 (2021) 2.
[28] P.J. Blau, Static and kinetic friction coefficients for selected materials, in, ASM Handbook (2018) 70–75.
[29] Coefficient of Friction- https://engineeringlibrary.org/reference/coefficient-of-friction.
[30] G. Sundararajan, N.M. Chavan, S. Kumar, The elastic modulus of cold spray coatings: Influence of inter-splat boundary cracking, J. Therm. Spray Technol. 22 (2013) 1348–1357, https://doi.org/10.1007/S11666-013-0034-5/METRICS.
[31] H.W. Swift, Plastic instability under plane stress, J. Mech. Phys. Solids 1 (1952) 1–18, https://doi.org/10.1016/0022-5096(52)90002-1.
[32] P. Hähner, C. Soyarslan, B. Gülçimen Çakan, S. Bargmann, Determining tensile yield stresses from Small Punch tests: A numerical-based scheme, Mater Des 182 (2019) 107974, https://doi.org/10.1016/J.MATDES.2019.107974.
[33] G. James, D. Witten, T. Hastie, R. Tibshirani, J. Taylor, An Introduction to Statistical Learning (2023), https://doi.org/10.1007/978-3-031-38747-0.
[34] P. Gao, C. Zhang, R. Wang, G. Deng, J. Li, L. Su, Tamping effect during additive manufacturing of copper coating by cold spray: A comprehensive molecular dynamics study, Addit. Manuf. 66 (2023) 103448, https://doi.org/10.1016/j.addma.2023.103448.
[35] A.A. Tiamiyu, C.A. Schuh, Particle flattening during cold spray: Mechanistic regimes revealed by single particle impact tests, Surf Coat Technol 403 (2020) 126386, https://doi.org/10.1016/j.surfcoat.2020.126386.
[36] M. Ashokkumar, D. Thirumalaikumarasamy, T. Sonar, S. Deepak, P. Vignesh, M. Anbarasu, An overview of cold spray coating in additive manufacturing, component repairing and other engineering applications, J Mech Behav Mater 31 (2022) 514–534, https://doi.org/10.1515/JMBM-2022-0056.
[37] B. Guerreiro, P. Vo, D. Poirier, J.-G. Legoux, X. Zhang, J.D. Giallonardo, Factors Affecting the Ductility of Cold-Sprayed Copper Coatings, J. Therm. Spray Technol. 29 (2020) 630–641, https://doi.org/10.1007/s11666-020-00993-z.
[38] S. Rasche, M. Kuna, Improved small punch testing and parameter identification of ductile to brittle materials, Int. J. Press. Vessel. Pip. 125 (2015) 23–34, https://doi.org/10.1016/j.ijpvp.2014.09.001.
[39] M. Bruchhausen, S. Holmström, I. Simonovski, T. Austin, J.M. Lapetite, S. Ripplinger, F. de Haan, Recent developments in small punch testing: Tensile properties and DBTT, Theor. Appl. Fract. Mech. 86 (2016) 2–10, https://doi.org/10.1016/J.TAFMEC.2016.09.012.
[40] E. Altstadt, M. Houska, I. Simonovski, M. Bruchhausen, S. Holmström, R. Lacalle, On the estimation of ultimate tensile stress from small punch testing, Int J Mech Sci 136 (2018) 85–93, https://doi.org/10.1016/J.IJMECSCI.2017.12.016.
[41] D. Petersen, R. Link, Y. Xu, Z. Zhao, A modified miniature disk test for determining material mechanical properties, J Test Eval 23 (1995) 300, https://doi.org/10.1520/JTE10429J.
[42] T.E. García, C. Rodríguez, F.J. Belzunce, C. Suárez, Estimation of the mechanical properties of metallic materials by means of the small punch test, J Alloys Compd 582 (2014) 708–717, https://doi.org/10.1016/j.jallcom.2013.08.009.
[43] D. Finarelli, M. Roedig, F. Carsughi, Small punch tests on austenitic and martensitic steels irradiated in a spallation environment with 530 MeV protons, J. Nucl. Mater. 328 (2004) 146–150, https://doi.org/10.1016/j.jnucmat.2004.04.320.
[44] Y.H. Zhang, W.Z. Han, Mechanism of brittle-to-ductile transition in tungsten under small-punch testing, Acta Mater 220 (2021) 117332, https://doi.org/10.1016/J.ACTAMAT.2021.117332.

[45] W. Li, D. Wu, K. Hu, Y. Xu, X. Yang, Y. Zhang, A comparative study on the employment of heat treatment, electric pulse processing and friction stir processing to enhance mechanical properties of cold-spray-additive-manufactured copper, Surf Coat Technol 409 (2021) 126887, https://doi.org/10.1016/J.SURFCOAT.2021.126887.

[46] Neeraj Sanjay Karmarkar, Characterization of Cold-Sprayed Copper Coatings and Comparison with Wrought Copper using Miniaturized Shear Punch Tests (SPT), Master of Science Thesis in Engineering in Manufacturing Systems Engineering, University of Michigan-Dearborn, 2018.

[47] R. Huang, M. Sone, W. Ma, H. Fukanuma, The effects of heat treatment on the mechanical properties of cold-sprayed coatings, Surf Coat Technol 261 (2015) 278–288, https://doi.org/10.1016/J.SURFCOAT.2014.11.017.